Ocean Engineering 73 (2013) 16–24

Contents lists available at ScienceDirect

Ocean Engineering

journal homepage: www.elsevier.com/locate/oceaneng

Numerical simulation of smart hydrofoil in marine system

M.H. Djavareshkian [a,*], A. Esmaeili [a], A. Parsania [b]

[a] Ferdowsi University of Mashhad, Iran
[b] Department of Mechanical Engineering, Payame Noor University, Tehran 19395-3697, Iran

ARTICLE INFO

Article history:
Received 14 July 2012
Accepted 13 July 2013

Keywords:
Smart shape
Hydrodynamic coefficients
Hydrofoil
Wave
Trochoid

ABSTRACT

A pressure-based implicit finite-volume technique is used to solve the Navier–Stocks equation, simulating flow around a smart hydrofoil. The Volume of Fraction (VOF) method is applied to track the free surface. This simulation focuses two main goals. Initially, the equation of a free surface wave, generated by the moving submerge hydrofoil, is extracted, and the wavelength and amplitude of the wave are assessed in the different submerge distances (h/c) and angle of flap (AOF). It is found that the trochoid equation predicts the free surface wave very well. Secondly, the simulation of fluid flow around the smart hydrofoil is performed, and its results are compared with the conventional hydrofoil. For both hydrofoils (smart and conventional), the effect of submerge distance and flap angle is evaluated. The results indicate that smart hydrofoils produce higher lift to drag ratio (L/D) than that of the conventional ones. Besides, the wave amplitude of smart hydrofoil is greater than conventional ones.

1. Introduction

Many smart aerodynamics and hydrodynamics configurations are still at the research and development stage, and their further commercial development depends on potential applications. They may provide solutions to existing problems or advanced technological possibilities that would otherwise not be feasible. Some smart configuration applications already exist in the aerodynamics of an airplane's wing (Bolonkin and Gilyard, 1999; Pern and Jacob, 1999; Campanile and Anders, 2005; Chinnasamy, 2006; Matsuzaki and Torii, 2006; Majji et al., 2007; Abdullah et al., 2009, 2010; Wickramasinghe et al., 2009). However, several studies are done to apply smart shape in the helicopter's blades (Anusonti-Inthra et al., 2005; Tiseo and Koopmann, 2006). Moreover, the aerodynamic of smart spoiler in racecar is performed (Djavareshkian and Esmaeli, 2012). Another application of smart structure can be considered in the aerodynamic of Wing in Ground vehicles (WIG) (M. Djavareshkian et al., 2011; M.H. Djavareshkian et al., 2011). Consequently, applied smart shape in the wind turbine is illustrated powerful influence on the aerodynamic performance (Barlas and Van Kuik, 2010). Therefore, almost all previous investigations have confirmed the beneficial implementation of smart configurations and have more experience of smart shapes that could be adapted for marine applications.

On the other hand, hydrofoils are widely utilized on ships and marine vehicles; furthermore, hydrofoil performance plays a significant role in the design of the vehicles. Therefore, increasing the performance can be affected on the ships and marine vehicles abilities (Kouh et al., 2002; Xie and Vassalos, 2007). Many ways and techniques can be utilized to increase hydrofoil performance. One of them is employing different optimization algorithms such as Neural Networks and Lagrange multiplier method (Schmitz et al., 2004; Hsin et al., 2006; Yang et al., 2009). Having high performance, the optimized hydrofoil can be worked in a special condition, and the change of mentioned condition causes to reduce the hydrofoil abilities. Therefore, to achieve maximum performance in all states, the shape of hydrofoil should be adapted, and it just becomes possible by using smart configurations in the hydrofoil surfaces. Up to now, using smart configurations in the marine vehicles is performed by Rediniotis et al. (1997, 2002), Quackenbush et al. (2005), Ming et al. (2009), and Wang et al. (2008). So far, the smart flap, which is applied smart structure as a hydrofoil's flap, is not considered, especially close to the water surface.

In this study, the hydrodynamic effects of using smart design in the hydrofoil's flap surfaces are numerically studied in which the hydrofoil moves near the water free surface. The smart hydrofoil is deflecting like fish body. Then, the comparison of smart and conventional flaps is numerically done. The effect of submerge distance and angle of the flap is performed, too. Another novelty of this paper is that the free surface wave equation is achieved, and the relationship between wavelength and amplitude of the wave is obtained for both hydrofoils (smart and conventional), various submerge distances and AOFs. Finally, a new equation for water wave is suggested, and its accuracy is studied.

* Corresponding author. Tel.: +98 511 8615100; fax: +98 511 8436432.
E-mail addresses: javareshkian@ferdowsi.um.ac.ir (M.H. Djavareshkian), aliesmaeli30316@yahoo.com (A. Esmaeili), a.parsania@farspnu.ac.ir (A. Parsania).

0029-8018/$ - see front matter © 2013 Elsevier Ltd. All rights reserved.
http://dx.doi.org/10.1016/j.oceaneng.2013.07.015

Nomenclature

VOF	Volume of Fraction
CFD	computational fluid dynamic
g	gravity acceleration
E	free surface wave velocity
j	wave number ($j=2\pi/\lambda$)
ε	turbulence model parameter
θ	angle (deg)
$\dot{m}$	mass transfer
c	cord length
L	lift force
D	drag force
CL	lift coefficient
CD	drag coefficient
I^c	convection flux
I^D	diffusion flux
SMA	shape memory alloy
h	submerge distance
AOF	angle of flap
AOA	angle of attack
A	cell face area
Re	Reynolds number
μ	dynamic viscosity
$\overrightarrow{S}$	source term
$V^{\rightarrow}$	velocity vector
t	time
ϕ	scalar quantity
G	generation term
H	water depth
2D	two dimensions
λ	wave length
σ	surface tension
α	volume fraction
k	turbulence model parameter
ω_0	weight/unit length (N/m)
$\bar{I}$	area moment of inertia (m^4)
B	length of the beam
x	horizontal cartesian coordinate
y	vertical cartesian coordinate
E	Young's modulus
ρ	density
p	pressure
Γ	diffusivity coefficient
$\overrightarrow{q}$	scalar flux vector
F	mass flux
$\overrightarrow{T}$	stress tensor
$\delta\nu$	cell volume
Fc	Froude number according chord length

2. Numerical solution setup and its conditions

2.1. Simulation smart flap deflection

Nature can learn some new approaches to expand technologies such as fish body and their abilities. If the hydrofoil surface can switch like fish, its performance can be raised. For this reason, it can be used a flap at the end of hydrofoil, so called a conventional hydrofoil. On the other hand, when smart materials are born, they may be applied to the flap structure of hydrofoil. The hydrofoil is named a smart hydrofoil. In this study, the smart flap deflection is designed with a cantilever beam so that the beam bending equation is the same as a smart flap chord deflection. Since the flap shape is a triangle, M. Djavareshkian et al. (2011) have considered it like a cantilever beams with uniformly varying load. The above-mentioned profile is given

$$y=\frac{\omega_0(-x^5+2B^2x^3-B^4x)}{120E\bar{I}B},\quad y_{Midline}=K(-x^5-ax^3+x)$$

$$M=\frac{1-B^4}{B^2} \tag{1}$$

2.2. Governing equations

The basic equations, which describe the conservation of mass, momentum and scalar quantities can be expressed in the following vector form, which is independent of the coordinate system.

$$\frac{\partial\rho}{\partial t}+div(\rho\overrightarrow{V})=S_m \tag{2}$$

$$\frac{\partial(\rho\overrightarrow{V})}{\partial t}+div(\rho\overrightarrow{V}\otimes\overrightarrow{V}-\overrightarrow{T})=\overrightarrow{S}_v \tag{3}$$

$$\frac{\partial(\rho\phi)}{\partial t}+div(\rho\overrightarrow{V}\phi-\overrightarrow{q})=\overrightarrow{S}_\phi \tag{4}$$

where ρ, $\overrightarrow{V}$ and ϕ are density, velocity vector and scalar quantity respectively, $\overrightarrow{T}$ is the stress tensor and $\overrightarrow{q}$ is the scalar flux vector. The latter two are usually expressed in terms of basic dependent variables. The stress tensor for a Newtonian fluid is defined as

$$\overrightarrow{T}=-P\overrightarrow{I} \tag{5}$$

In addition, the Fourier-type law gives the scalar flux vector:

$$\overrightarrow{q}=\Gamma_\phi grad\phi \tag{6}$$

In this study, $k-\varepsilon$ model is used for turbulence flow.

$$\frac{\partial}{\partial t}(\rho k)+\frac{\partial}{\partial x_j}\left(\rho u_j k-\Gamma_k\frac{\partial k}{\partial x_j}\right)=G-\rho\varepsilon \tag{7}$$

$$\frac{\partial}{\partial t}(\rho\varepsilon)+\frac{\partial}{\partial x_j}\left(\rho u_j\varepsilon-\Gamma_\varepsilon\frac{\partial\varepsilon}{\partial x_j}\right)=C_1\frac{\varepsilon}{k}G-C_2\rho\frac{\varepsilon^2}{k} \tag{8}$$

The turbulent viscosity and diffusivity coefficients are defined as

$$\mu_t=C_\mu\rho\frac{k^2}{\varepsilon} \tag{8}$$

$$\Gamma_\phi^t=\left(\frac{\mu_t}{\sigma_\phi^t}\right) \tag{10}$$

Moreover, the generation term G in Eqs. (7) and (8) is defined as

$$G=\mu_t\left[\left(\frac{\partial u_i}{\partial x_j}+\frac{\partial u_j}{\partial x_i}\right)\frac{\partial u_i}{\partial x_j}\right] \tag{11}$$

The discretization of the above differential equations is carried out by using a finite-volume approach. First, the solution domain is divided into a finite number of discrete volumes or cells, where all variables are stored at their geometric centers.

The equations are then integrated over all the control volumes by utilizing the Gaussian theorem. The discrete expressions are presented to refer to only one face of the control volume, namely, e, for the sake of brevity. For any variable of ϕ (which may also stand

for the velocity components), the result of the integration yields is formed as

$$\frac{\partial \nu}{\partial t}\left[(\rho\phi)_p^{n+1}-(\rho\phi)_p^n\right]+I_e-I_w+I_n-I_s=S_\phi\delta\nu \tag{12}$$

where I's are the combined cell-face convection I^c and diffusion I^D fluxes. The diffusion flux is approximated by central differences. The discretization of the convective flux requires a particular attention, and it causes to develop the various schemes. A representation of the convective flux for cell-face (e) is

$$I_e^c=(\rho VA)_e\phi_e=F_e\phi_e \tag{13}$$

The value of ϕ_e is not known, and it should be estimated from the values at neighboring grid points by interpolation. The expression for the ϕ_e is determined by Second order Upwind scheme. The final form of the discretized equation from each approximation is given as

$$A_p\phi_p=\sum_{m=E,W,N,S}A_m\phi_m+S_\phi^{'} \tag{14}$$

where A's are the convection–diffusion coefficients. The term $S_\phi^{'}$ in Eq. (14) contains quantities arising from non-orthogonality, numerical dissipation terms and external sources. For the momentum equations, it is easy to separate out the pressure-gradient source from the convection momentum fluxes.

The VOF idea has been used to simulate two-phase fluid (water and air). This idea can model two or more immiscible fluids by solving a particular set of momentum equations and tracking the volume fraction of each of the fluids throughout the domain. The tracking of the interface between two phase is accomplished by the solution of a continuity equation for the volume fraction of one of them. For the qth phase, this equation has the following form:

$$\frac{1}{\rho_q}\left[\nabla(\alpha_q\rho_q\vec{v})=S_{\alpha q}+\sum_{p=1}^{n}(\dot{m}_{pq}-\dot{m}_{qp})\right] \tag{15}$$

where $\dot{m}_{pq}$ is the mass transfer from phase q to phase p and $\dot{m}_{qp}$ is the mass transfer from phase p to phase q. $S_{\alpha q}$ is the source term so that is equal zero in this problem. The volume fraction equation will not be solved for the primary phase. The primary-phase volume fraction will be computed based on the following constraint:

$$\sum_{q=1}^{n}\alpha_q=1 \tag{16}$$

The volume fraction equation may be solved either through implicit or explicit discretization. In this research, implicit is used.

2.3. Solution algorithm

Most contemporary pressure-based methods employ a sequential iteration technique in which the different conservation equations are solved one after another. The common approach in enforcing continuity is taken by combining the equation for continuity with those of momentum to derive an equation for pressure or pressure-correction. The present work employs the SIMPLE technique in which the implicit discretized equations are solved by a sequence of predictor and corrector steps.

2.4. Grid strategy and domain property

In the numerical simulation, grid and domain independence and a comparison of current result and published data should be investigated. In the present research, two-dimensional (2D) hydrofoil that it is moving near the free surface of water has been studied. In order to verify the solution, a simulation of flow has been performed around the hydrofoil with NACA4412 section.

Fig. 1 demonstrates the boundary condition. At the inlet (left side) for both air and water, velocity is prescribed. At the outlet (right side) of them, the pressure has a constant value. Slip boundary conditions are utilized on top and bottom faces of the domain and wall boundary conditions are used for hydrofoil surfaces. According to this, the dimensions of domain are chosen after doing several different lengths.

The grid type in the simulation is created by a structured mesh, because of its simplicity and applicability to the current flow configuration (i.e., with a nearby free surface). In this process, H-type grid is used; subsequently, the schematic shape of the 2D mentioned grid is shown in Fig. 2. The grid independence is found by doing several different trials and the effect of grid sizing is illustrated in Fig. 3; finally, a grid with 84,000 cells is selected as independent grid. In other cases, the above process is utilized for grid and domain independences.

Table 1 illustrates the setting of numerical simulation. Because of two phase flow simulation and moving hydrofoil near the free surface of water, Froude number is considered according to hydrofoil chord (Fc).

To validate the simulation, Fig. 4 indicates the pressure coefficient distribution on the NACA4412 hydrofoil surfaces for an AOA$=5^\circ$ and $h/c=1$. Comparisons demonstrate that the numerical results are in a good argument with published experimental data (Kouh et al., 2002). Subsequently, Table 2 draws an analogy between the lift coefficient for the present calculation and experimental value on the different Froude numbers, and it can be drawn the conclusion that the numerical results are in a high-quality adaptation with experimental data. Consequently, the

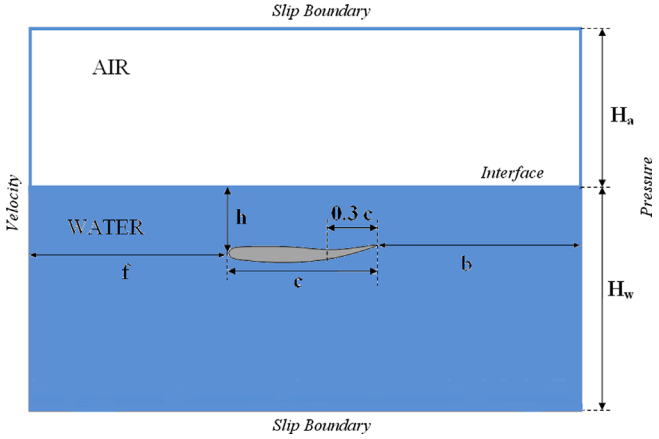

Fig. 1. Dimension and boundary condition of 2D domain.

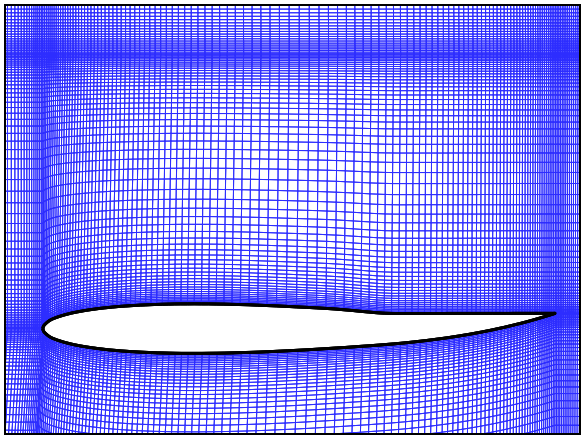

Fig. 2. H grid topology and H grid around the hydrofoil.

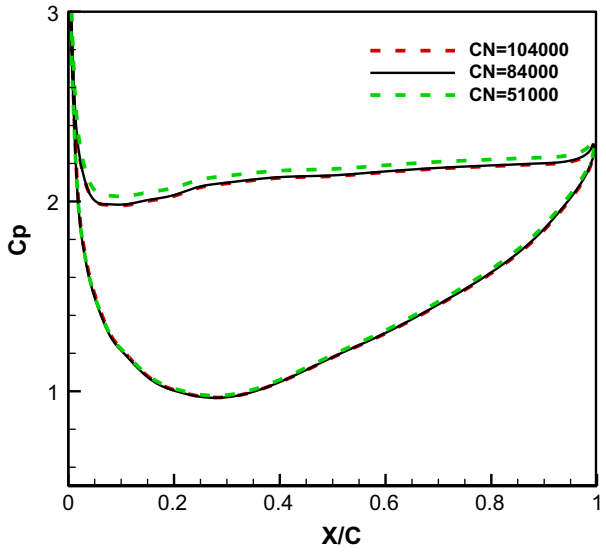

Fig. 3. Effect of grid sizing on pressure distribution on the surface of the NACA4412 hydrofoil for an AOA=5°, Fc=1 and $h/c=1$.

Table 1
Settings for numerical simulation.

Flow	Turbulent
Solver	2-D double precision
Momentum equation	Second order Upwind
Solver	SIMPLE
Turbulent model	$k-\varepsilon$

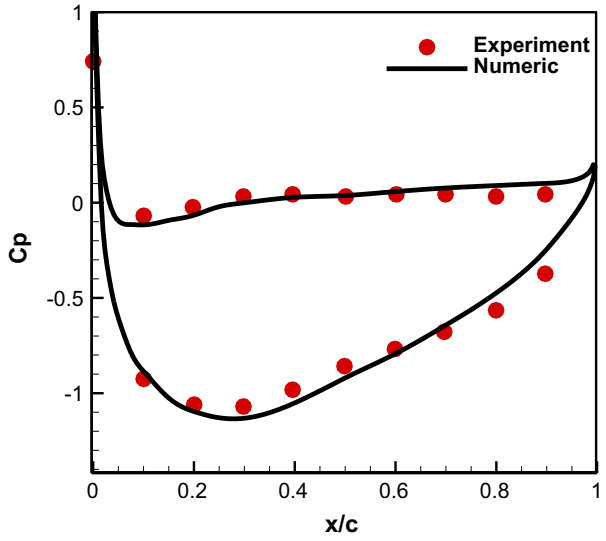

Fig. 4. Comparison between numerical and experimental pressure coefficient distribution around the NACA4412, AOA=5° and $h/c=1$.

Table 2
Comparison of numerical and experimental lift coefficients.

Fc	CL (numerical)	CL (experimental)	Error (%)
0.8	0.9946	1.094	9.00
1	0.7585	0.7441	1.93
1.2	0.6525	0.6202	5.21
1.4	0.5705	0.5654	0.90
1.6	0.5412	0.5522	1.99
1.8	0.5266	0.5481	3.92

mesh characteristics and simulation parameters for current cases have been chosen according to this simulation.

3. Results and analysis

In this research, numerical simulation of flow around the smart and conventional hydrofoils with flap has been performed. However, the simulation of hydrofoils has been analyzed at 7 different angles of attack, −7.5°, −5°, −2.5°, 0.0°, 2.5°, 5° and 7.5°; moreover, the submerge distance falls into 3 main categories, 0.5, 0.7 and 1, for both smart and conventional cases. The Reynolds and Froude numbers are 3.1×10^6 and 1, respectively.

Firstly, the equation of wave, which is generated by moving the hydrofoil near the free surface of water, is achieved. According to the last investigations, the shape of an ocean wave is often depicted as a sinusoidal wave, but the experimental and numerical wave shapes that observed by naval architects proves other shapes. Therefore, a new approach is needed to find the best equation of the wave. Accordingly, several equations are tested to discover the best matched equation with the wave. As a result, it is found out that a trochoid equation has more harmony with the water surface wave in all of the conditions. The equation is generated by a fixed point within a circle when it rolls along and under a straight line. Parametric equation of the trochoid is defined as

$$\left\{\begin{array}{l} x=a\theta-b\sin(\theta) \\ y=a-b\cos(\theta) \end{array}\right\} \tag{17}$$

where θ is the variable angle, through which the circle rolls. Value (a) is illustrative wavelength and parameter (b) is demonstrative amplitude. To verify the accuracy of the equation, the actual wave, obtained from this numerical simulation, is compared with the trochoid equation (Fig. 5). The excellent adjustment between them proves the high accuracy of the trochoid equation to predict the wave shape. In addition, this figure makes a comparison of actual wave and trochoid equation for smart and conventional hydrofoils. It can be concluded that this equation is extremely suitable even different types of hydrofoil. The trochoid wave equation, which is formed by moving the smart and conventional hydrofoils under

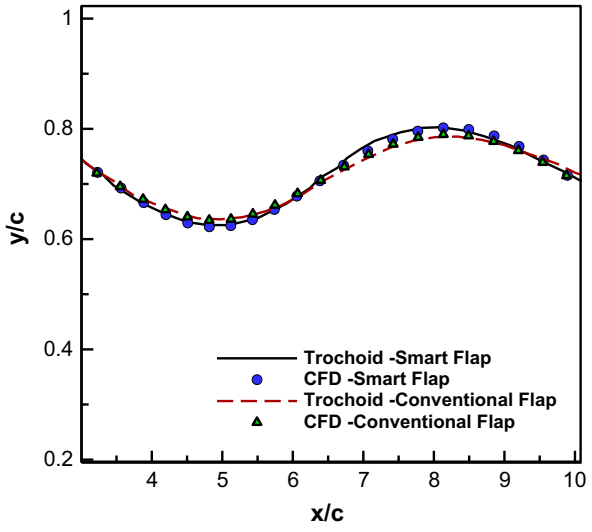

Fig. 5. Comparisons of actual wave and trochoid equation for smart and conventional hydrofoils in $h/c=0.5$.

water for AOF=+7.5° and $h/c=0.7$, is shown as

$$\text{Smart hydrofoil} \begin{Bmatrix} x = 1.050\,\theta - 0.090\sin(\theta) \\ y = 1.050 - 0.090\cos(\theta) \end{Bmatrix} \quad (18)$$

$$\text{Conventional hydrofoil} \begin{Bmatrix} x = 1.050\,\theta - 0.078\sin(\theta) \\ y = 1.050 - 0.078\cos(\theta) \end{Bmatrix} \quad (19)$$

Moreover, comparison of actual and trochoid wave shapes in a variety of AOF is depicted in Fig. 6; whereas, it leads to acclaim the equation. The figure proves that trochoid equation is highly suitable, even if the flap angle is changed.

Another contribution of this investigation is to develop smart shape in hydrofoil configuration and how effects on its performance. According to Eqs. (18) and (19), (a) coefficient for two types of hydrofoil is equal; therefore, it can be found that kind of hydrofoil does not affect on wavelength. On the other hand, the

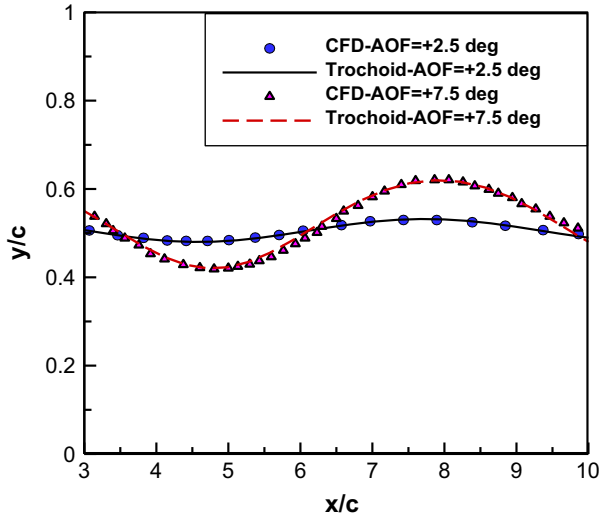

Fig. 6. Comparisons of CFD and trochoid wave shape due to moving smart hydrofoil in $h/c=0.5$.

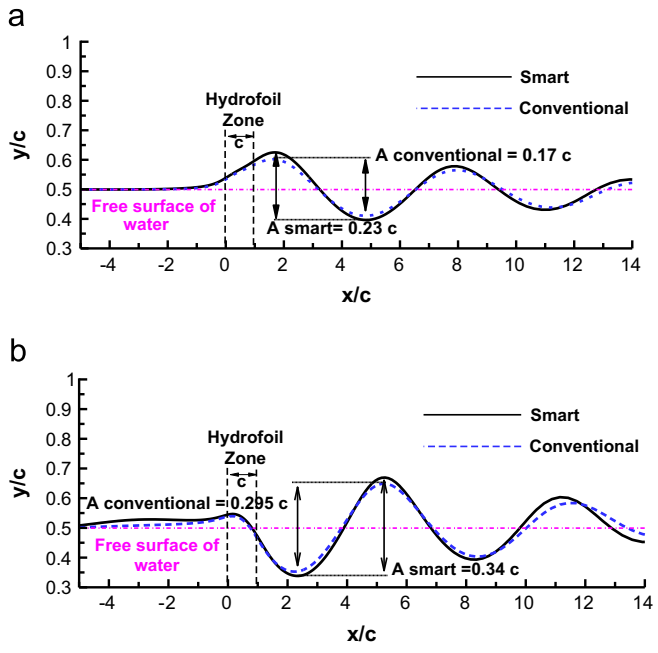

Fig. 7. Comparisons of wave shape of smart and conventional hydrofoils for $h/c=0.5$. (a) AOF=+7.5° and (b) AOF=−7.5°.

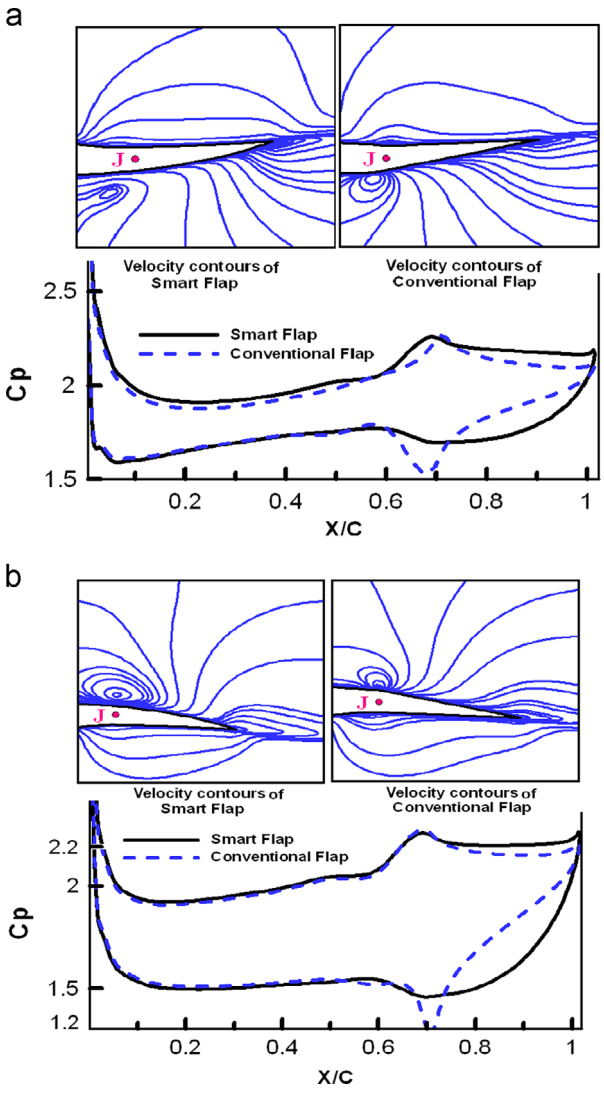

Fig. 8. Comparison of pressure coefficient distribution on smart and conventional hydrofoil surface for $h/c=1.0$. (a) Positive deflection (AOF=+7.5) and (b) negative deflection (AOF=−7.5).

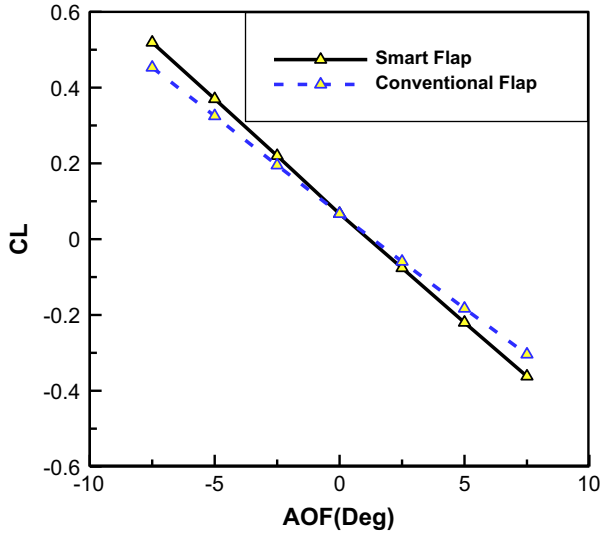

Fig. 9. Variations of CL between smart and conventional hydrofoil as a function of AOF for $h/c=1.0$.

(b) coefficient for smart hydrofoil is higher than that of the conventional ones; hence, wave amplitude has increased in a smart hydrofoil.

The wave shape may be influenced by various AOF and the impact of them can recognize some valuable points. For that reason, the wave shape of smart and conventional hydrofoils in $h/c=0.5$ and different AOF are compared in Fig. 7(a) and (b). The figure demonstrates that wavelength is constant for both of them. The reason for these differences can be interested and it can be discovered in wave velocity. Wavelength depends on the nature of the wave and its parameters, such as wave velocity, depth, surface tension. The wave velocity has been obtained by

$$E^2=\frac{g}{j}\left(1+\sigma\frac{j^2}{\rho g}\right)\tanh(jH) \tag{20}$$

In this study, the wave velocity is equal the speed of hydrofoil and has a constant value for all cases. Furthermore, σ, g and ρ are constants because of being water inherent properties. Hence, wavelength is independent of the hydrofoil types.

The water wave amplitude is also the key factor in the comparison of the smart and conventional hydrofoils. Fig. 7 (a) demonstrates that the amplitude is $0.17c$ in the conventional and $0.23c$ in the smart hydrofoils; consequently, the smart hydrofoils have a stronger amplitude than others do. These differences are due to a pressure disturbance on the hydrofoil surfaces. Subsequently, Fig. 8 illustrates the pressure coefficient distribution on the both hydrofoil's surfaces and demonstrates the pressure difference between upper and lower surfaces of the smart hydrofoil is higher than that of the conventional ones. As the result of this, the smart hydrofoil generates waves with high amplitude. Comparison of the pressure coefficient distributions gives some benefit views that the use of a smart flap is conducted a moderate pressure gradient in the junction of the flap to the hydrofoil. It can be seen that the pressure difference between upper and lower surfaces of hydrofoil in the smart flap region is higher than that of in the conventional ones, and there is an undershooting in the pressure distribution at the connection of conventional flap to the hydrofoil.

To compare well between two types of hydrofoil, the behavior of down force (lift) and drag coefficients would be studied; whereas, Fig. 9 illustrates variations of lift coefficient as a function of AOF. It can be found that the absolute of lift coefficient and slope of its curve in the smart hydrofoil are more than in the conventional ones. Moreover, Fig. 10 demonstrates the amount of drag coefficient, generated by the smart hydrofoil, is more than that of in conventional ones. It also indicates that the use of a smart flap gives more variation in the drag force against conventional ones.

The mean reason of high drag coefficient in the smart hydrofoil can be investigated in Figs. 11 and 12. The figures show distributions of mean velocity in the boundary layer of the flap zone and wake region behind the hydrofoil. Fig. 11(a) indicates that the velocity on the bottom flap side of the smart hydrofoil is more than that of the conventional ones, and the inverse is true for the velocity on the top flap surfaces. Furthermore, the smart hydrofoil leads to generate a stronger wake than the conventional ones (see e.g. Fig. 11(b)). This behavior is similarity seen in the positive deflection cases. Fig. 12(a) makes a comparison of the velocity

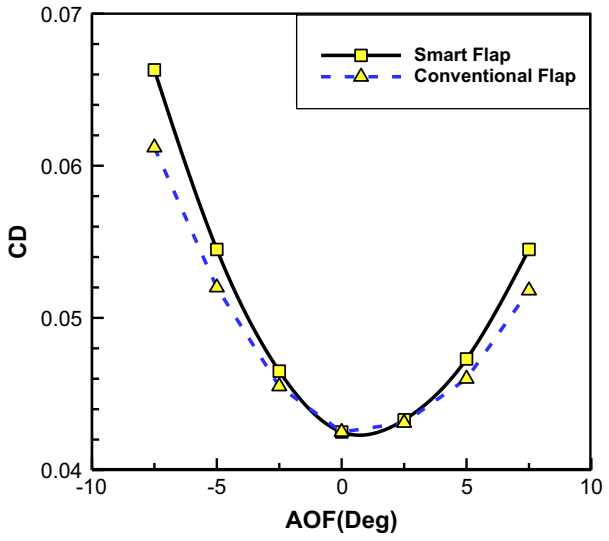

Fig. 10. Variations in CD as a function of AOF for smart and conventional flap for $h/c=1.0$.

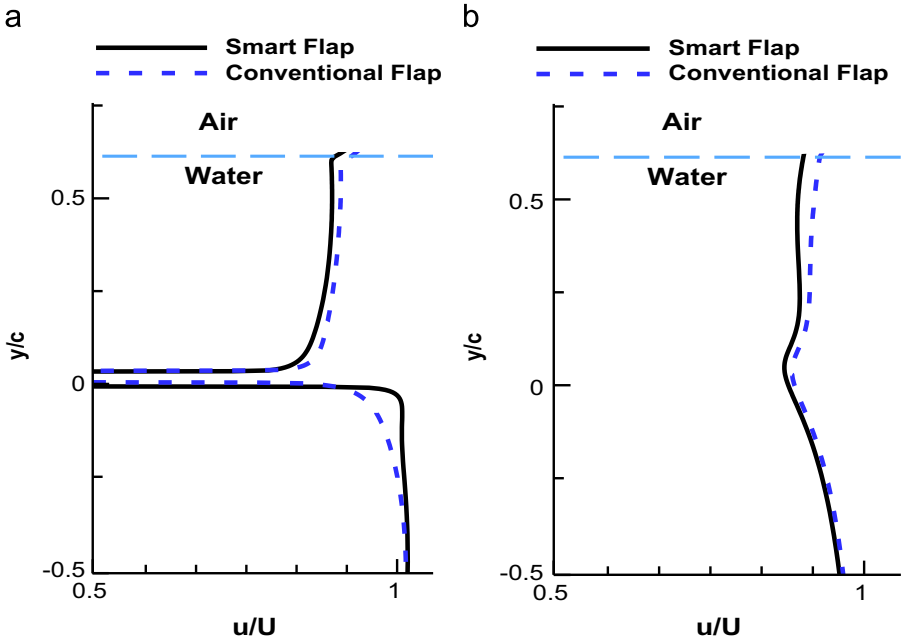

Fig. 11. Velocity profile (a) on the middle of flap zone and (b) behind the hydrofoil for AOF=+7.5° and $h/c=0.5$. (a) $X/C=0.85$ and (b) $X/C=2.0$.

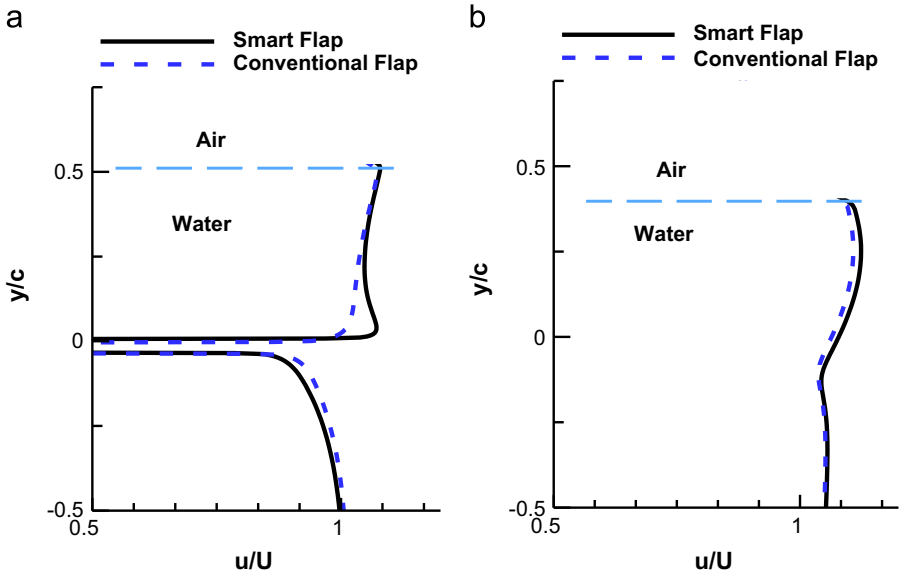

Fig. 12. Velocity profile (a) on the middle of flap zone and (b) behind the hydrofoil for AOF= −7.5° and h/c=0.5. (a) X/C=0.85 and (b) X/C=2.0.

difference between upper and lower surfaces of the smart and conventional hydrofoils and the difference is more noticeable in the smart hydrofoil.

Lift to drag ratio (L/D) plays a pivotal role in the hydrofoil design. The absolute value of L/D for positive deflection has been presented in Fig. 13(a), and it is depicted that L/D is on the rise when the AOF and h/c have been slightly increased. In addition, the upward trend is highlighted for AOF=5° and 7.5° whereas, the L/D is nearly a constant value as varying depth for AOF=2.5°. Another remarkable change involves fluctuation of L/D in the negative deflections as shown in Fig. 13(b). In this figure, the L/D has been moderately increased by the growth of AOF and h/c. As the result of these, the amount of L/D in the smart hydrofoil is rather high when is compared to that of in the conventional ones. Consequently, using smart configuration in the hydrofoil structure as a flap is more effective on the hydrofoil performance especially in comparison with the traditional hydrofoils. It can be appreciated that the smart hydrofoils will be valuable equipment in the design of marine vehicles.

The effect of flap angle can set out some powerful arguments, which will shape the vision of the hydrofoil performance. As it said, the AOF is divided into 7 segments from upward to downward deflections, −7.5°, −5°, −2.5°, 0.0°, 2.5°, 5° and 7.5°. Fig. 14 indicates the wave shape, generated by the smart hydrofoil, for various AOF. It can be seen that the flap angle does not mutate the wavelength, whereas effects on the wave amplitude. The wave equations for different AOF are given as (in h/c=0.5)

$$\mathrm{AOF} = +2.5^{\circ}\left\{\begin{array}{l} x = 1.000\theta - 0.026\sin(\theta) \\ y = 1.000 - 0.026\cos(\theta) \end{array}\right\} \tag{21}$$

$$\mathrm{AOF} = +7.5^{\circ}\left\{\begin{array}{l} x = 1.000\,\theta - 0.100\sin(\theta) \\ y = 1.000 - 0.100\cos(\theta) \end{array}\right\} \tag{22}$$

The equations broadly support the views that the wavelength is independent of AOF versus, the variations of AOF play a vital role in the amplitude of waves, so that the amplitude for AOF=+2.5° is lower than that of for AOF=+7.5°. The views establish a connection between the characteristics of the wave and flap surface curvature. In addition, the shape of the water surface is following the flap surface curvature and the wave has formed according to change in the flap surfaces.

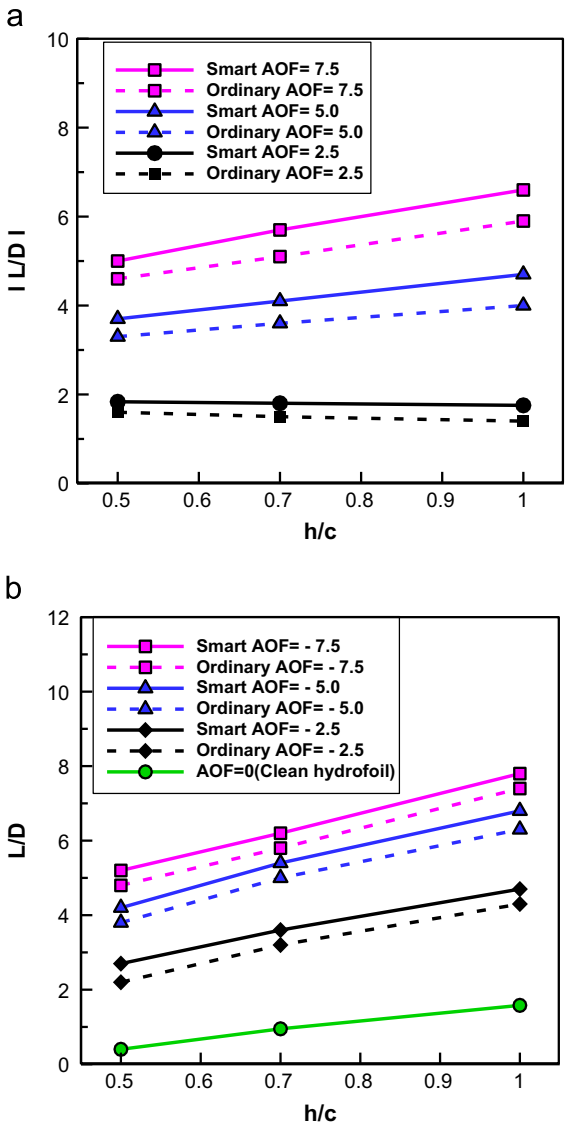

Fig. 13. Variations in L/D as a function of h/c for different submerged depth. (a) Positive deflection and (b) negative deflection.

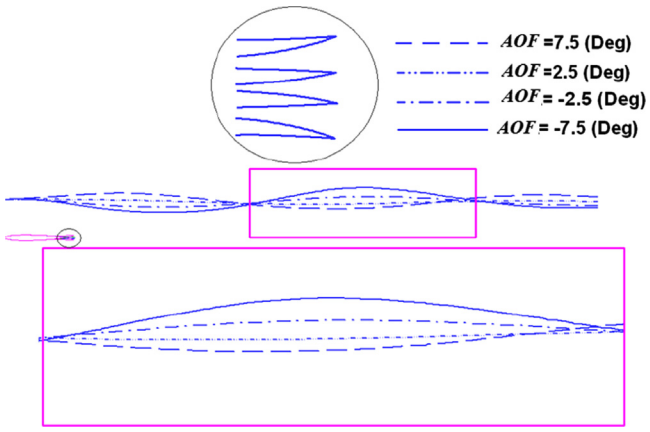

Fig. 14. Water surface wave shape for different AOF due to submerge hydrofoil for $h/c=0.5$.

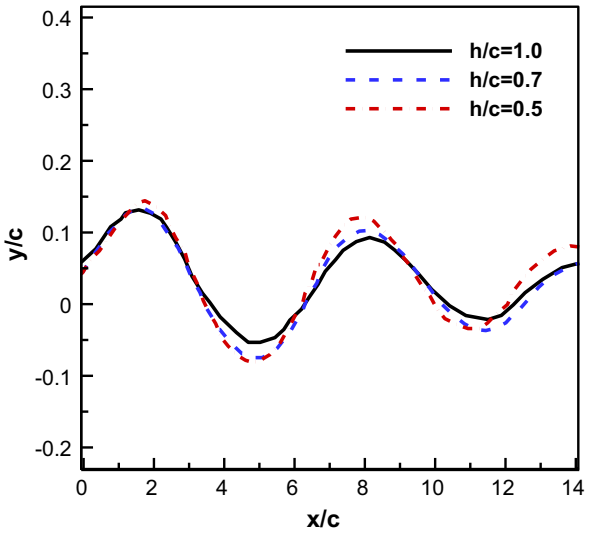

Fig. 15. Wave generated for different h/c and AOF=+7.5°.

Final effective parameter on the hydrofoil performance is the submerge distance (h/c), which is exposed in Fig. 15. It lays emphasis on relating characteristics of the wave and h/c, whereas the wave amplitude has dramatically surged by a falling of h/c, and the reverse is true for wavelength. On the other hand, the wavelength is slightly reduced by a decrease of h/c. The feeble wave (small amplitude) makes reference to a low pressure between the upper surface of hydrofoil and the water surface. To understand better, velocity contours around a hydrofoil for different submerge distances are shown in Fig. 16(a)–(c). These figures indicate that the velocity has been slightly declined by the reduction of h/c. This is due to flow blockage between the upper surface of hydrofoil and the water free surface. Therefore, pressure on the hydrofoil's upper surface would be high when the hydrofoil is closed to the water surface.

The variations of lift coefficient according to the h/c demonstrate that the lift force is increased when the submerge distance (h/c) becomes more (Table 3). The lift coefficient is due to buoyancy and hydrodynamic forces. The buoyancy force has obtained from

$$L_{Buoyancy}=\rho Vg$$

$$CL_{Buoyancy}=L_{Buoyancy}/(0.5\rho U^2)$$

$$CL_{Hydrodynamic}=CL_{Total}-CL_{Buoyancy} \quad (23)$$

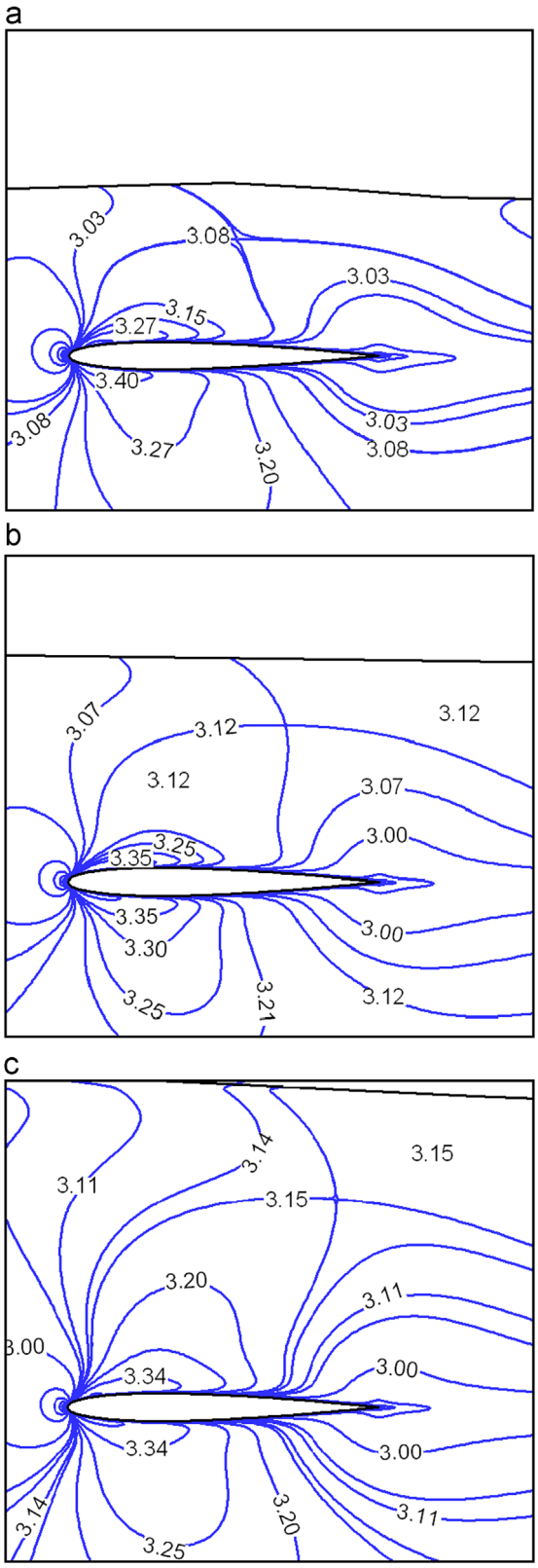

Fig. 16. Velocity contours around the hydrofoil for AOF=0. (a) $h/c=0.5$, (b) $h/c=0.7$ and (c) $h/c=1$.

According to Eq. (23), the buoyancy lift force has a constant value because of having the same shape of hydrofoil in all cases. On the other hand, the absolute of hydrodynamic lift force is slightly declining by an increase of h/c. Pursuant to following sentences, pressure between the upper surface of hydrofoil and the water surface has

Table 3
Lift component of Symmetrical hydrofoil.

	CL_{Total}	$CL_{Buoyancy}$	$CL_{Hydrodynamic}$ (pressure & friction)
$h/c=0.5$	0.017	0.124	−0.107
$h/c=0.7$	0.040	0.124	−0.080
$h/c=1.0$	0.067	0.124	−0.057

reduced, and a weak wave has been generated in the deeper submerge distance (h/c); but pressure on the upper surface of hydrofoil has grown. Therefore, the absolute of hydrodynamic lift force has moderately fallen. Consequently, the total lift coefficients have a dramatic upsurge according to increasing h/c (Table 3).

4. Conclusion

A pressure-based implicit finite-volume procedure is utilized to solve the Navier–Stocks, simulating flow around the smart hydrofoil and Volume of Fraction (VOF) method is applied to track the free surface. The equation of a free surface wave due to moving submerge hydrofoil is extracted, and the wavelength and amplitude of wave are assessed for different submerge distance (h/c), angle of flap (AOF) and hydrofoil types (conventional and smart flaps). The main findings can be summarized as follows:

(1) Trochoid equation is extremely adaptive for free surface waves.
(2) The hydrofoil type does not effect on wavelength, but a smart hydrofoil generates a high wave amplitude when is compared with a conventional ones.
(3) The wavelength for different AOFs is equal, but the wave amplitude for a small AOF is lower than that of a high AOF.
(4) The amount of L/D for smart hydrofoil is higher than that of for conventional ones. Consequently, using smart configuration in the hydrofoil structure as a flap is more effective on the hydrofoil performance especially in comparison with the traditional hydrofoils.

Acknowledgments

This work was supported in part by Ferdowsi University of Mashhad's Research Council, under grant #265 (dated 28-06-2011) on 'Static Fine Job'.

References

Abdullah E., Bil C. and Watkins S., Numerical simulation of an adaptive airfoil system using SMA actuators, 48th AIAA Aerospace Sciences Meeting Including the New Horizons Forum and Aerospace Exposition, 2010, 4–7.

Abdullah, E.J., Bil, C., Watkins, S., 2009. Application of Smart Materials for Adaptive Airfoil Control. American Institute of Aeronautics and Astronautics, 1801 Alexander Bell Dr., Suite 500 Reston, VA 20191-4344, USA.

Anusonti-Inthra, P., Gandhi, F., Frecker, M., 2005. Design of a conformable rotor airfoil using distributed piezoelectric actuation. AIAA Journal 43 (8), 1684–1695.

Barlas, T., Van Kuik, G., 2010. Review of state of the art in smart rotor control research for wind turbines. Progress in Aerospace Sciences 46 (1), 1–27.

Bolonkin, A., Gilyard, G.B., Center, H.L.D.F.R., Aeronautics, U.S.N., Administration, S., 1999. Estimated Benefits of Variable-Geometry Wing Camber Control for Transport Aircraft. National Aeronautics and Space Administration, Dryden Flight Research Center.

Campanile, L.F., Anders, S., 2005. Aerodynamic and aeroelastic amplification in adaptive belt-rib airfoils. Aerospace Science and Technology 9 (1), 55–63.

Chinnasamy, P., 2006. Application of Computational Fluid Dynamics on Smart Wing Design. University of Nevada, Las Vegas.

Djavareshkian, M.H., Esmaeli, A., 2012. Application of smart flap for race car wings. International Journal of Academic Development 2 (1), 66–92.

Djavareshkian, M., Esmaeli, A., Parsani, A., 2011. Aerodynamics of smart flap under ground effect. Aerospace Science and Technology 15, 642–652.

Djavareshkian, M.H., Esmaeli, A., Parsania, A., Ziaforoughi, A., 2011. Three-dimensional investigation of smart flap aerodynamics for a WIG vehicle. Transactions of the Japan Society for Aeronautical and Space Science, Aerospace Technology Japan 9, 51–60.

Hsin, C.Y., Wu, J.L., Chang, S.F., 2006. Design and optimization method for a two-dimensional hydrofoil. Journal of Hydrodynamics B 18 (3), 323–329.

Kouh, J., Lin, T., Chau, S., 2002. Performance analysis of two dimensional hydrofoil under free surface. Journal of National Taiwan University 86 (10), 113–123.

Majji, M., Rediniotis, O.K., Junkins, J.L., 2007. Design of a morphing wing: modeling and experiments. In: Proceedings of AIAA Atmospheric Flight Mechanics Conference and Exhibit, South Carolina.

Matsuzaki, Y., Torii, H., 2006. Flutter boundary prediction of an adaptive smart wing during process of adaptation using steady-state response data. In: Proceedings of 47th AIAA/ASME/ASCE/AHS Structures, Structural Dynamics, and Materials Conference, Rhode Island.

Ming, A., Park, S., Nagata, Y., Shimojo, M., 2009. Development of underwater robots using piezoelectric fiber composite. In: Proceedings of IEEE International Conference on Robotics and Automation, Kobe, pp. 3821–3826.

Pern, N.J., Jacob, J., 1999. Wake Vortex Mitigation Using Adaptive Airfoils, vol. 57. AIAA, pp. 167–177.

Quackenbush, T., Carpenter, B., Gowing, S., 2005. Design and Testing of a Variable Geometry Ducted Propulsor Using Shape Memory Alloy Actuation. AIAA Paper 1077.

Rediniotis, O.K., Lagoudas, D.C., Mashio, T., Garner, L.J., Qidwai, M.A., 1997. Theoretical and experimental investigations of an active hydrofoil with SMA actuators. Journal of Intelligent Material Systems and Structures 277–289.

Rediniotis, O., Wilson, L., Lagoudas, D.C., Khan, M., 2002. Development of a shape-memory-alloy actuated biomimetic hydrofoil. Journal of Intelligent Material Systems and Structures 13 (1), 35–49.

Schmitz, A., Besnard, E., Hefazi, H., 2004. Automated Hydrodynamic Shape Optimization Using Neural Networks.

Tiseo, B., Koopmann, G., 2006. Smart Tunable Dynamic Vibration Absorbers. In: Proceedings of 12th AIAA/CEAS Aeroacoustics' Conference, 27th AIAA Aeroacoustics' conference. Cambridge, Massachusetts: American Institute of Aeronautics and Astronautics, 1801 Alexander Bell Drive, Suite 500, Reston, pp. 20191–24344.

Wang, Z., Hang, G., Wang, Y., Li, J., Du, W., 2008. Embedded SMA wire actuated biomimetic fin: a module for biomimetic underwater propulsion. Smart Materials and Structures 17, 025039.

Wickramasinghe, V.K., Chen, Y., Martinez, M., Kernaghan, R., Wong, F., 2009. Design and Verification of a Smart Wing for an Extremely-Agile Micro-Air-Vehicle. American Institute of Aeronautics and Astronautics, 1801 Alexander Bell Dr., Suite 500 Reston, VA 20191-4344, USA.

Xie, N., Vassalos, D., 2007. Performance analysis of 3D hydrofoil under free surface. Ocean Engineering 34 (8), 1257–1264.

Yang, S., Xi, W., Ma, L., Zhang, H., Yang, Z., 2009. Optimizing-computation of controlling parameters of intelligent propulsion system of a hydrofoil sliding craft propelled by adjustable-pitch screw. In: Proceedings of IEEE, pp. 1815–1818.